

Metallicity in the merger Seyfert galaxy NGC 6240

M. Contini

School of Physics and Astronomy, Tel Aviv University, Tel Aviv 69978, Israel

Accepted: Received ; in original form 2010 month day

ABSTRACT

We have calculated the physical conditions throughout the merger Seyfert galaxy NGC 6240 by modelling the observed optical and infrared line ratios. We have found that the optical spectra are emitted by clouds photoionised by the power-law radiation flux from the AGN (or AGNs), and heated mainly by the shock accompanying the propagation of the clouds outwards. The infrared line ratios are emitted from clouds ejected from a starburst which photoionises the gas by the black-body radiation flux corresponding to a stellar colour temperature of about 5×10^4 K. Both the flux from the AGN and the ionization parameters are low. The most characteristic physical parameters are the relatively high shock velocities ($\geq 500 \text{ km s}^{-1}$) and low preshock densities ($\sim 40\text{--}60 \text{ cm}^{-3}$) of the gas. The C/H, N/H, O/H relative abundances are higher than solar by a factor ≤ 1.5 . We suggest that those relative abundances indicate trapping of H into H_2 molecules rather than high metallicities. Adopting an initial grain radius of $1 \mu\text{m}$, the dust temperatures calculated in the clouds reached by the power-law radiation and by the black-body radiation are 81 K and 68 K, respectively.

Key words: radiation mechanisms: general — shock waves — ISM: abundances — galaxies: Seyfert — galaxies: individual: NGC 6240

1 INTRODUCTION

Colliding galaxies are at first identified by the morphological appearance of the encounter, depending on the merging evolution age, but they are hardly recognizable through the physical properties of the new galaxy. Eventually, the spectra show the dominant role of dynamical processes such as shock waves and starbursts created by collision, yet the active galactic nuclei (AGNs) have a dominant role.

Evidences of galaxy collision in the Seyfert galaxy NGC 6240 appeared on prints of the Palomar Sky Survey (Fosbury & Wall 1979, hereafter FW79), namely, a complex high luminosity structure with substantial plumes extending over 130 kpc, large dust lanes and chaotic appearance of the nuclear region. The synchrotron characteristic of the radio emission, the coincidence of a central feature seen in the optical ($\text{H}\alpha$ + [NII] emission) with radio emission, the strength of the low level ionization lines reveal the presence of shock waves as a result of collision. FW79 in fact suggested that the NGC 6240 system is the result of an encounter between galaxies. They dismissed the hypothesis that the collision could trigger star formation, comparing the observed line ratios with those emitted from gas ionized by the black body radiation flux from young stars.

On the other hand, Rieke et al. (1985) defined NGC 6240 as a site of exceedingly powerful bursts of star forma-

tion, involving nearly $10^{10} M_{\odot}$ of newly formed stars. This was suggested not only by the luminosity and extent of the stellar component near $2 \mu\text{m}$, but particularly on the basis of the large population of red supergiants required to account for the depth of the stellar CO absorption.

NGC 6240 was definitively classified among mergers by Fried & Schulz (1983) who detected a "pronounced" double nucleus on an S1 image tube plate in the I band and on r and I exposures taken with a CCD camera. The two nuclei are oriented at a position angle of 10° and separated by $1.8''$ ($640\text{--}700$ pc, projected on the sky) with diameters of $2.5''$ and $1.5''$.

Fried & Schulz claimed that both nuclei appear to be non-stellar, rejecting the hypothesis of an accidental projection of a foreground star. The extended regions observed by them are dominated by shock heating on a scale of ~ 6 kpc. The binary active nucleus in NGC 6240 was confirmed by Komossa et al (2003). Using CHANDRA, they discovered two hard X-ray nuclei coincident with the optical-IR ones. Each nucleus host an AGN detected in hard X-rays and at 5 GHz (Gallimore & Beswick 2004).

A starburst in NGC 6240 is the source of the K-band luminosity, dominated by supergiants (Tecza et al. 2000). The starburst was triggered quite recently and has a duration time less than 5 million yrs. It fills the central kpc, the region encompassing the two nuclei (Engel et al 2010).

Heckman et al. (1990) showed evidence of a starburst driven super-wind on a large scale ($> \text{kpc}$).

At a distance of 97 Mpc ($z=0.0245$, $H_0=75 \text{ km s}^{-1} \text{ Mpc}^{-1}$), NGC 6240 has an infrared luminosity $L_{\text{IR}} \sim 10^{11.8} L_{\odot}$ (Engel et al 2010). It was included in the list of ultra-luminous infrared galaxies (ULIRGs) by Rigopoulou et al. (1999). The dynamical field is characterised by the extraordinary large stellar velocity dispersions ($\sim 350 \text{ km s}^{-1}$). The optical spectrum of NGC 6240 shows many emission lines with line ratios characteristic of a collisional dominated regime rather than a power-law radiation dominated flux generally prevailing in the narrow line region (NLR) of AGN (FW79).

The mid-infrared (IR) spectrum taken with the Infrared Spectrograph on the *Spitzer Space Telescope* by Armus et al (2006) shows the flux of the most significant strong fine-structure lines up to $[\text{SiII}] 34.8 \mu\text{m}$, as well as rotational H_2 lines and PAH emission features. Armus et al inquired about the buried AGN contribution to the bolometric luminosity. The mid-IR spectrum was included in the survey of the AGN NLR in the IR by Dasyra et al (2011).

Comparing mid-infrared emission-line properties from high-resolution Spitzer spectra of a hard X-ray (14-195 keV) selected sample of nearby ($z < 0.05$) AGNs detected by the Burst Alert Telescope (BAT) aboard Swift, Weaver et al. (2010) found that the luminosity distribution of the $[\text{O IV}] 25.89 \mu\text{m}$, $[\text{Ne II}] 12.81 \mu\text{m}$, $[\text{Ne III}] 15.56 \mu\text{m}$, and $[\text{Ne V}] 14.32, 24.32 \mu\text{m}$ lines and hard X-ray continuum are similar for Seyfert 1 and Seyfert 2 populations. They also found that the emission lines primarily arise in gas ionized by the AGNs. On the other hand, Luhman et al. (1998) report measurements of the $[\text{C II}] 157.74 \mu\text{m}$ fine-structure line in ULIRGs with the Long Wavelength Spectrometer on the Infrared Space Observatory. They claim that the observation of $[\text{CII}]/\text{FIR}$ continuum ratio is consistent with starburst nuclei.

In this paper we investigate the source of radiation and the physical conditions of the emitting gas in NGC 6240 by a detailed modelling of the optical spectrum presented by FW79 and of the mid-IR spectrum reported by Armus et al.

The clumpy and irregular morphology of NGC 6240 and the relatively large FWHM of the spectral lines indicate that, besides the photoionization flux from the AGNs, shocks are heating and ionizing the NLR gas. The leading role of shocks was already noticed by FW79 on the basis of the strong neutral and low level ionization lines. Indeed, different regions throughout merging galaxies show physical conditions changing on small scales (e.g. for NGC 7212 and NGC 3393). The spectrum observed from NGC 6240 is an average of the spectra emitted from the different regions. Trying to disentangle various components throughout a unique spectrum leads to approximated results. However, the rather peculiar line ratios observed by FW79 suggest that the task is worthy. We will refer to the observed spectra with the maximum precision as we have done for other merger galaxies (e.g. NGC 3393, Contini 2012, NGC 7212, Contini et al 2012, MKN 298, Radovich et al. 2005), i.e. trying to find some records of collision analysing the spectra. A first hint can be obtained by modelling the spectral line ratios and the spectral energy distribution (SED) of the continuum. Our aim, in particular, is to distinguish the

contribution of the AGN from that of the starbursts in a strongly dominated shock wave regime.

We will adopt composite models which account for the flux from the active centre (AC) and/or for radiation from the stars, consistently coupled with shock wave hydrodynamics. We have found in previous investigations (e.g. Rodríguez-Ardila et al. 2005, Contini et al. 2004a, Viegas et al. 1999, and references therein) that, not only shocks are important to explain high ionization level lines (e.g. $[\text{FeVII}]$, $[\text{FeX}]$) coronal lines (e.g. $[\text{SiVIII}]$, $[\text{SiIX}]$) as well as low ionization and neutral lines (e.g. $[\text{OI}]$ and $[\text{NI}]$), but also they determine the intensity and the frequency of the SED peaks in the X-ray and IR domains.

We have run a grid of models in order to select the most appropriated one reproducing the NGC 6240 observed line ratios. Building the grid by many models we could explore which ranges of the physical parameters could characterise the NLR of NGC 6240.

The calculations of the spectra are presented in Sect. 2. The optical spectrum presented by FW79 and the fine-structure line ratios in the IR observed by Armus et al. are investigated in Sect. 3. The calculated continuum SED is compared with the observational data in Sect. 4. Discussion and concluding remarks follow in Sect. 5.

2 THE CALCULATION CODE

In this paper, the line and continuum spectra emitted by the gas downstream of the shock front are calculated by the code SUMA¹. The code simulates the physical conditions in an emitting gaseous cloud under the coupled effect of photoionization from an external radiation source and shocks. The line and continuum emission from the gas are calculated consistently with dust-reprocessed radiation in a plane-parallel geometry.

2.1 Input parameters

The input parameters which refer to the shock, are represented by the shock velocity V_s , the pre-shock density n_0 , the pre-shock magnetic field B_0 . The input parameter that refers to the radiation field is the power-law flux from the active center F in number of photons $\text{cm}^{-2} \text{ s}^{-1} \text{ eV}^{-1}$ at the Lyman limit, if the photoionization source is an active nucleus, and the spectral indices $\alpha_{UV}=-1.5$ and $\alpha_X=-0.7$. F is combined with the ionization parameter U by

$U = (F/(n c (\alpha - 1))) ((E_H)^{-\alpha+1} - (E_C)^{-\alpha+1})$ (Contini & Aldrovandi, 1983), where E_H is H ionization potential and E_C is the high energy cutoff, n the density, α the spectral index, and c the speed of light.

If stars with a colour temperature T_* are the photoionization source, the number of ionizing photons $\text{cm}^{-2} \text{ s}^{-1}$ produced by the hot source is $N = \int_{\nu_0} B_{\nu}/h\nu d\nu$, where $\nu_0 = 3.29 \cdot 10^{15} \text{ Hz}$ and B_{ν} is the Planck function. The flux from the star is combined with U and n by $N (r/R)^2 = U n c$, where r is the radius of the hot source (the stars), R is the radius of the nebula (in terms of the distance from the stars), n is the density of the nebula and c is the speed of light. Therefore,

¹ <http://wise-obs.tau.ac.il/~marcel/suma/index.htm>

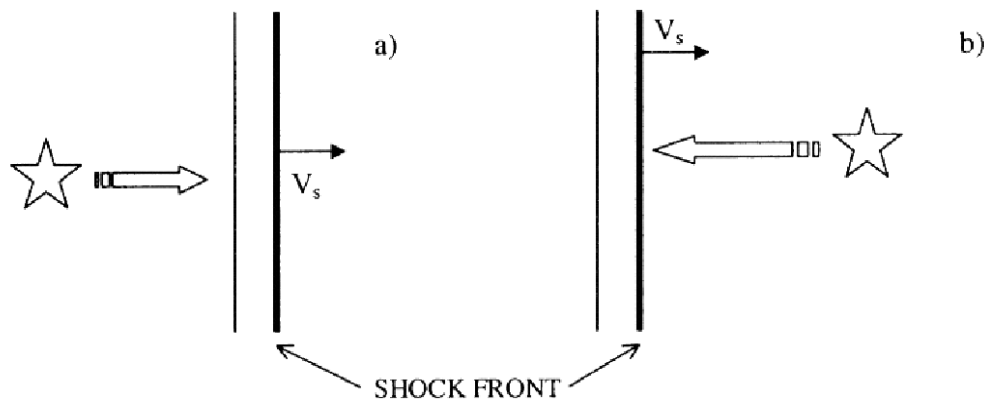


Figure 1. Case a) : the cloud withdraws from the external radiation source which is represented by the star; case b) the cloud approaches the radiation source

T_* and U compensate each other, but only in a qualitative way, because T_* determines the frequency distribution of the primary flux, while U represents the number of photons per number of electrons reaching the nebula. The choice of T_* and U is made by the fit of the line ratios.

The secondary diffuse radiation emitted from the slabs of gas heated by the shocks is also calculated. The flux from the active center or from the stars (primary radiation) and the secondary radiation are calculated by radiation transfer throughout the slabs downstream.

The dust-to-gas ratio (d/g) and the abundances of He, C, N, O, Ne, Mg, Si, S, A, Fe relative to H, are also accounted for. They affect the calculation of the cooling rate. The dust grains are heated radiatively by photoionization and, collisionally, by the shock. Changing d/g will change the mutual heating and cooling of gas and dust. The distribution of the grain radii downstream results from sputtering.

The geometrical thickness of the emitting nebula D , determines whether the model is radiation-bound or matter-bound.

2.2 Calculation process

The calculations start at the shock front where the gas is compressed and thermalized adiabatically, reaching the maximum temperature in the immediate post-shock region ($T \sim 1.5 \times 10^5 (V_s / 100 \text{ km s}^{-1})^2$). T decreases downstream following recombination. The cooling rate is calculated in each slab. The downstream region is cut up into a maximum of 300 plane-parallel slabs with different geometrical widths calculated automatically, in order to account for the temperature gradient (Contini 2009 and references therein).

In each slab, compression is calculated by the Rankine–Hugoniot equations for the conservation of mass, momentum and energy throughout the shock front. Compression (n/n_0) downstream ranges between 4 (the adiabatic jump) and ≥ 100 , depending on V_s and B_0 . The stronger the magnetic field, the lower the compression downstream, while a higher shock velocity corresponds to a higher compression.

The ionizing radiation from an external source is characterized by its spectrum and by the flux intensity. The flux is calculated at 440 energies, from a few eV to keV. Due to radiative transfer, the spectrum changes throughout the downstream slabs, each of them contributing to the optical

depth. In addition to the radiation from the primary source, the effect of the diffuse radiation created by the gas line and continuum emission is also taken into account, using 240 energies to calculate the spectrum.

For each slab of gas, the fractional abundance of the ions of each chemical element is obtained by solving the ionization equations. These equations account for the ionization mechanisms (photoionization by the primary and diffuse radiation, and collisional ionization) and recombination mechanisms (radiative, dielectronic recombinations), as well as charge transfer effects. The ionization equations are coupled to the energy equation when collision processes dominate and to the thermal balance if radiative processes dominate. The latter balances the heating of the gas due to the primary and diffuse radiations reaching the slab with the cooling due to recombinations and collisional excitation of the ions followed by line emission, dust collisional ionization and thermal bremsstrahlung. The coupled equations are solved for each slab, providing the physical conditions necessary for calculating the slab optical depth, as well as its line and continuum emissions. The slab contributions are integrated throughout the cloud.

In particular, the absolute line fluxes referring to the ionization level i of element K are calculated by the term $n_K(i)$ which represents the density of the ion $X(i)$. We consider that $n_K(i) = X(i)[K/H]n_H$, where $X(i)$ is the fractional abundance of the ion i calculated by the ionization equations, $[K/H]$ is the relative abundance of the element K to H and n_H is the density of H (by number cm^{-3}). In models including shock, n_H is calculated by the compression equation (Cox 1972) in each slab downstream. So the abundances of the elements are given relative to H as input parameters.

Dust grains are coupled to the gas across the shock front by the magnetic field. They are heated by radiation from the AGN and collisionally by the gas to a maximum temperature which is a function of the shock velocity, of the chemical composition and of the radius of the grains, up to the evaporation temperature ($T_{\text{dust}} \geq 1500 \text{ K}$). The grain radius distribution downstream is determined by sputtering, which depends on the shock velocity and on the density. Throughout shock fronts and downstream, the grains might be destroyed by sputtering.

Summarizing, the code starts by adopting an initial gas electron temperature $T_e (\sim 10^4 \text{ K})$ and the input parameters

for the first slab (Sect. 2.1). Then, it calculates the density from the compression equation, the fractional abundances of the ions from each level for each element, line emission, free-free emission and free-bound emission. It re-calculates T_e by thermal balancing or the enthalpy equation, and calculates the optical depth of the slab and the primary and secondary fluxes. Finally, it adopts the parameters found in slab i as initial conditions for slab $i+1$. By integrating the contribution of the line intensities calculated in each slab, we obtain the absolute fluxes of each of the lines, calculated at the nebula (the same for bremsstrahlung). We then calculate the line ratios to a certain line (in the present case $H\beta$ for the optical spectrum which is a strong line), and we compare them with the observed line ratios.

In particular, the code accounts for the direction of the cloud motion relative to the external photoionizing source (Fig. 1). If the radiation flux from the source reaches the shock front edge of the cloud, the switching parameter $str=0$, whereas when the flux reaches the edge opposite to the shock front, $str=1$. In the former case the calculations start at the shock front and proceed until the gas is at a temperature below 10^3 K (the model is radiation bound) or the calculations are interrupted when all the lines reproduce the observed line ratios (the model is matter bound).

In the latter case, i.e. when the cloud propagates outwards from the radiation source, the calculations require some iterations, until the results converge. In the first iteration a shock dominated model is adopted ($F=0$). We start from the shock front in order to calculate the profile of the density downstream. The ionization equations account only for the secondary radiation and collisional ionization. The density as well as the secondary radiation are stored for each of the slabs. The temperatures calculated in the first iteration are stored only in the region of the cloud where collision processes prevail. They will be used in the following iteration.

In the second iteration the calculations start from the edge of the cloud reached by the external radiation flux. The primary and secondary radiation fluxes are calculated by radiation transfer throughout each slab and are adopted for the resolution of the ionization equation system. The secondary radiation from the photoionized side of the cloud is stored for each slab.

In the following iteration all the process is recalculated starting from the shock front using the primary flux stored in the previous iteration and the secondary radiation from both sides of the cloud. It is clear that the cloud geometrical thickness plays an important role. Figs. 2 and 3 show that, if the cloud is very thin, the cool gas region may disappear leading to $[OI]=0$ and $[NI]=0$.

3 MODELLING THE LINE SPECTRA

We start by modelling the line spectra because they are more constraining than the continuum SED. In fact, the line ratios depend on the stratification of the ions downstream, that is very specific for each model. On the other hand, the bremsstrahlung shows the characteristic trend for gas at temperatures $\leq 10^4$ K common to all the models at frequencies lower than 10^{14} Hz. In the UV range it is generally blended with the strong black body emission corresponding

to the old star population background. Only the maximum frequency of the bremsstrahlung peak depends directly on the shock velocity.

3.1 Selection of the models

The physical parameters are combined throughout the calculation of forbidden and permitted lines emitted from a shocked nebula. The ranges of the physical conditions in the nebula are deduced, as a first guess, from the observed lines.

Generally, the shock velocity is determined by both a close approximation to the observed FWHM of the line profiles and the best fit to the observed line intensities (~ 400 – 500 km s $^{-1}$ for NGC 6240). A high V_s increasing compression downstream, speeds up the cooling rate, leading to enhanced low ionization level lines.

The [NI] 5200+ (the + indicates that the doublet is summed up) lines constrain the model because the critical density for collisional deexcitation of the lines is very low (< 2000 cm $^{-3}$). Considering that compression (n/n_0) downstream is between ~ 50 and >100 for relative high shock velocities, a low n_0 (< 100 cm $^{-3}$) is predicted. The [OII] 3727+ and [SII] 6717+ lines can also be drastically reduced by collisional deexcitation at high electron densities ($n_e > 3000$ cm $^{-3}$).

Adopting a composite model (shock + photoionization) some interesting issues should be explained. We fit the spectral lines adopting an n_0 which is combined with the other input parameters, including the preshock magnetic field B_0 . The magnetic field has an important role in models accounting for the shock. The stronger B_0 the lower the compression. So, lower densities are compensated by a lower magnetic field. We have adopted $B_0 = 10^{-4}$ G, which is suitable to the NLR of AGN (Beck 2011).

In pure photoionization models, the density n is constant throughout the nebula, while in a shock wave regime, n is calculated downstream by the compression equation in each of the single slabs. Compression depends on n , the magnetic field B and the shock velocity V_s . In models accounting for the shocks, both the electron temperature T_e and the electron density n_e are far from constant throughout each cloud, showing the characteristic profiles in the downstream region (see Figs. 2 and 3). In particular, throughout each cloud, the density reaches its upper limit downstream and remains nearly constant, while the electron density decreases following recombination. A high density, increasing the cooling rate, speeds up the recombination process of the gas, enhancing neutral lines. In fact, each line is emitted from a region of gas at a different n_e and T_e , depending on the ionization level and the atomic parameters characteristic of the ion. So, even sophisticated calculations reproduce approximately the highly inhomogeneous conditions of the gas, leading to some discrepancies between calculated and observed line ratios.

The radiation intensity of the flux from the AGN is evaluated from the [OIII]/[OII] line ratios. The higher F , the higher [OIII]/[OII]. Moreover, a high F maintains the gas ionized far from the source yielding enhanced [OI] and [SII] lines. Recall that these lines behave similarly because S first ionization potential (10.36 eV) is lower than that of O (13.61 eV).

The geometrical thickness (D) of the emitting clouds

is mainly determined by $[\text{OI}]/\text{H}\beta$ because $[\text{OI}]$ is emitted from gas at relatively low temperature, at the cloud edge opposite to the shock front in the inflow case, or in the centre of the cloud for the outflow case (see Figs. 2 and 3). The geometrical thickness of a cloud establishes whether a model is radiation-bound or matter-bound. A first analysis of the data in NGC 6240 shows that the models are mostly radiation-bound.

The parameters are intermingled therefore the effect of a single parameter on the final spectrum is not always straightforward, particularly for outflow models in which the low and intermediate ionization level lines come from both sides of the cloud (Figs. 2 and 3).

During the modelling process, if a satisfactory fit is not found for all the lines, a new iteration is started with a different set of input parameters. When a line ratio is not reproduced, we check how it depends on the physical parameters and we decide consequently how to change them. Each line ratio has a different weight. We generally consider that the observed spectrum is satisfactorily fitted by a model when the strongest line ratios are reproduced by the calculation within a 20% discrepancy and weak line ratios within 50%.

The final gap between observed and calculated line ratios is due to the observational errors both random and systematic, as well as to the uncertainties of the atomic parameters adopted by the code, such as recombination coefficients, collision strengths etc., which are continuously updated, and to the choice of the model. The final model is constrained by the SED of the continuum.

Summarizing, the parameters within a certain range derive from the line ratios. Then they are refined phenomenologically by the detailed modelling of the spectrum. The set of the input parameters which leads to the best fit of the observed line ratios determines the physical and chemical properties of the emitting gas. These are the "results" of our calculations.

3.2 Comparison of calculated with observed line ratios

We will consider first the optical spectrum which shows oxygen lines from three ionization levels constraining the choice of the models.

3.2.1 The optical lines

The spectrum observed by FW79 is reported in Table 1 (top panel, second column). It was taken with the Anglo-Australian Telescope at 3.6m ESO. The absorption line redshift corresponds to a Hubble distance of 145 Mpc, adopting $H_0 = 50 \text{ km s}^{-1}/\text{Mpc}$ (FW79). The line FWHM corresponds to $700 \pm 100 \text{ km s}^{-1}$ after correction for instrumental broadening. The nuclear region of the galaxy suffers substantial extinction. The equivalent width of $\text{H}\beta$ emission after correction for $A_V = 4 \text{ mag}$, corresponds to an observed flux above the atmosphere of $1.7 \cdot 10^{-14} \text{ erg cm}^{-2} \text{ s}^{-1}$. The isotropic luminosity in the rest frame of the source is $1.8 \cdot 10^{42} \text{ erg s}^{-1}$.

The spectrum shows many emission lines from low ionization species. The $[\text{OII}]/[\text{OIII}] > 6$ line ratios ($[\text{OII}]/\text{H}\beta = 12.3$ and $[\text{OIII}]/\text{H}\beta = 1.6$) are unusually high in AGN, even for a shock dominated regime.

In the FW79 observed spectrum $\text{H}\alpha$ and $[\text{NII}]6548+6584$ lines are summed up, whereas the calculated $\text{H}\alpha$ and the $[\text{NII}] 6548+6584$ line ratios to $\text{H}\beta$ are given separately. In fact, $[\text{NII}] 6548+6584/\text{H}\beta$ is important to determine the N/H relative abundance. We can predict that in the observed corrected spectrum $\text{H}\alpha / \text{H}\beta \sim 3$ for gas in the NLR physical conditions. In fact, in reddening corrected spectra emitted by gas at relatively low densities ($\sim 10^3 - 10^4 \text{ cm}^{-3}$) $\text{H}\alpha / \text{H}\beta$ ranges between 3.10 for $T_e = 5000 \text{ K}$ and 2.86 for $T_e = 10,000 \text{ K}$ (Osterbrock 1989). Unfortunately in NGC 6240 the $[\text{SII}]6716, 6731$ doublet which indicates the density of the emission gas, is not resolved.

In Table 1 we compare model results with the optical spectrum observed and corrected by FW97 in the top panel. The optical line ratios refer to $\text{H}\beta = 1$. The absolute flux of $\text{H}\beta$ calculated by the models is given in the last row of the top panel. In the bottom section of Table 1, we present the input parameters adopted by the models, followed by the relative abundances C/H, N/H and O/H which show some variance from the solar ones ($\text{C}/\text{H} = 3.3 \cdot 10^{-4}$, $\text{N}/\text{H} = 9.1 \cdot 10^{-5}$, $\text{O}/\text{H} = 6.6 \cdot 10^{-4}$, $\text{Ne}/\text{H} = 10^{-4}$, $\text{Mg}/\text{H} = 2.6 \cdot 10^{-5}$, $\text{S}/\text{H} = 1.6 \cdot 10^{-5}$, $\text{Fe}/\text{H} = 3.2 \cdot 10^{-5}$ Allen 1976).

We try to reproduce the $[\text{OIII}]5007+/\text{H}\beta$ line ratio which is rather weak in NGC 6240, by readjusting in particular F and V_s . Then, we consider $[\text{OII}]/\text{H}\beta$, which depends on V_s and n_0 . The $[\text{OII}]3727+$ doublet is very strong compared with the spectra emitted from the NLR of AGNs. This suggests that the flux from the active center is low ($\log F \leq 9$). Therefore, a shock dominated regime is predicted, which is characterised by relatively high $[\text{OII}]/[\text{OIII}] (\geq 1)$. This does not mean that photoionization is negligible, in fact the active nuclei have been observed. Relatively high $[\text{OI}]/\text{H}\beta$ shows that the models are radiation-bound.

The models which reproduce approximatively the data were selected among hundreds in a large grid. It is expected that the large number of the code input parameters may induce degeneracy, namely different combinations of the parameters could lead to many models reproducing the data within the accepted ranges (within 20% for strong lines and 50 % for weaker lines). As a matter of fact, a degeneracy can arise, for example, from the density and the magnetic field which are directly correlated, but in the present modelling we use $B_0 = 10^{-4} \text{ gauss}$ for all models. Moreover, the line intensities I_λ result from integration ($I_\lambda = \sum \Delta I_\lambda$) on the cloud slabs downstream which reach a maximum number of 300 and vary from model to model. The ΔI_λ for each ion is calculated adopting density, temperature and flux calculated in the specific slab. So the probability of finding the same spectrum for different sets of input parameters is very low. We give in the Appendix a selection of models, which give a hint about the role of the different parameters. We refer to the oxygen line ratios $[\text{OIII}]5007+/\text{H}\beta$, $[\text{OII}]3727+/\text{H}\beta$ and $[\text{OI}]6300+/\text{H}\beta$. The grid in Table A1 shows that only two models reproduce these line ratios by 9%, 28% and 53% (model $m2_{pl}$) and by 2%, 58% and 15% (model $m1_{pl}$). Models $m1_{pl}$ and $m2_{pl}$ are reported in Table 1. They were calculated adopting outflow of the cloud from the galaxy centre.

We show in Table 1 also a model corresponding to a relatively high velocity ($m0_{pl}$), selected from the grid (Table A1) which represents the case of inflow. This case is less probable

Table 1. Comparison of calculated with observed spectra

line	obs ¹	m1 _{pl}	m0 _{pl}	m2 _{pl}	m0 _{sb}	m1 _{sb}	m2 _{sb} ²	m _{AV} ³
[OII] 3727+	12.3	12.	11.	11.2	10.	9.	9.3	10.
[NeIII] 3869+	0.31	0.79	0.92	0.76	0.06	0.45	0.4	0.475
H γ	0.34	0.44	0.45	0.45	0.46	0.45	0.45	0.45
[OIII] 4363	<0.25	0.32	0.38	0.18	0.026	0.24	0.2	0.2 2
H β	1.	1.	1.	1.	1.	1.	1.	1.
[OIII] 5007+	1.8	4.28	5.5	2.5	2.	3.	2.6	2.6
[NI] 5200	0.43	0.27	0.38	1.8	0.002	0.08	0.2	0.54
[NII] 5755	< 0.10	0.096	0.08	0.07	0.04	0.07	0.07	0.07
[OI] 6300+	1.41	1.2	1.47	3.	0.006	0.4	0.9	1.2
H α + [NII] 6584+	8.25	3.3+5.12	3.1+5.5	3.1+5.3	3.+5.	3.2+3.7	3.2 +5.	3+5.0
[SII] 6716+	2.62	1. + 1.2	1.6+1.7	1.8+1.7	0.2+0.23	0.74+0.93	0.24+0.32	1.2
H β (erg cm ⁻² s ⁻¹)	1.7e-14	1.18e-3	1.1e-3	1.15e-3	8.8e-3	1.3e-3	1.9e-3	-
[ArII] 6.98	0.3	0.20	0.22	0.25	0.035	0.18	0.26	0.26
[SIV] 10.5	0.02	0.04	0.04	0.046	0.026	0.035	0.007	0.014
[NeII] 12.8	1.	1.	1.	1.	1.	1.	1.	1.
[NeV] 14.3	0.048	0.046	0.05	0.038	0.036	0.049	0.04	0.04
[NeIII] 15.5	0.32	1.95	2.22	2.7	0.29	0.39	0.4	0.8
[SIII] 18.7	0.103	1.83	0.93	1.6	1.7	0.73	0.3	0.7
[NeV] 24.3	< 0.02	0.06	0.07	0.05	6.3e-3	0.07	0.05	0.05
[OIV] 25.9	0.2	0.33	0.35	0.28	0.23	0.31	0.25	0.25
[FeII] 26	0.12	2.18	1.9	2.06	0.08	1.28	0.19	0.5
[SIII] 33.48	0.14	3.14	1.1	2.1	1.47	0.81	0.5	0.8
[SiII] 34.8	1.4	7.5	6.2	6.0	0.42	3.	3.6	4.
[NeII] 12.8 (erg cm ⁻² s ⁻¹)	193.1e-14	1.04e-3	1.e-3	7.2e-4	5.6e-3	9.6e-4	1.4e-3	-
[CII] 158 (erg cm ⁻² s ⁻¹)	2.57e-12	1.18e-3	1.2e-3	2.9e-4	2.8e-4	1.7e-4	8.3e-4	-
V _s (km s ⁻¹)	-	900	900	500	300	500	500	-
n ₀ (cm ⁻³)	-	40	40	40	60	60	68	-
F ⁴	-	3.e8	3.e8	3.e8	-	-	-	-
U	-	-	-	-	0.06	0.002	0.002	-
T _* (K)	-	-	-	-	3.e4	5.e4	5.e4	-
D (cm)	-	6.e17	1.23e17	1.e17	9.e16	1.e19	1.e19	-
str	-	1	0	1	0	1	1	-
C/H	-	4.3e-4	3.3e-4	4.3e-4	4.3e-4	4.3e-4	4.3e-4	-
N/H	-	1.5e-4	1.5e-4	1.5e-4	1.5e-4	1.5e-4	1.5e-4	-
O/H	-	9.6e-4	8.6e-4	8.6e-4	9.6e-4	9.6e-4	9.6e-4	-

¹ data in the optical come from Fosbury & Wall (1979), in the mid-IR from Armus et al (2006). [CII] 158 comes from Luhman et al (1998); the absolute flux of H β , [NeII] 12.8 and [CII] 158 are observed at Earth but the models are calculated at the nebula.

² calculated by Si/H=2.e-5, S/H=4.e-6, Ar/H=8.3e-6 and Fe/H=3.e-6.

³ calculated by a relative weight of 0.3 for model m2_{pl} and of 0.7 for model m2_{sb}.

⁴ in number of photons cm⁻² s⁻¹ eV⁻¹ at the Lyman limit

considering the starburst super-wind on a large scale predicted by Heckman et al. (1990). Moreover, the calculated [OIII]5007+/H β disagrees from the observed line ratio by ~ 70%.

Models m1_{pl} and m2_{pl} represent clouds ionized and heated by the power-law (pl) flux from the AC. They both correspond to a relatively low flux ($F=3 \cdot 10^8$ in number of photons cm⁻² s⁻¹ eV⁻¹ at the Lyman limit), a relatively low preshock density $n_0=40$ cm⁻³ and represent clouds propagating outward from the AC, although with different velocities ($V_s = 900$ and 500 km s⁻¹, respectively). Recall that shocks are also accounted for in radiation dominated models.

So far we have discussed the spectra emitted from clouds photoionised by the AGN. However, the starburst in NGC 6240 is also a strong photoionization source.

Models m1_{sb} and m0_{sb}, represent outflow from the starburst and inflow, respectively. The m2_{sb} model represents

also outflow in the starburst case. We will address it regarding the IR lines. The inflow case must be dropped because underpredicts by some orders of magnitude the [OI]/H β line ratios, as was predicted by FW79. The model representing gas ejected from the starburst, m1_{sb} is more appropriated to the physical picture, but it reproduces the [OII]/H β , [OIII]/H β and [OI]/H β line ratios by 27 %, 55 % and 72 %, respectively. Although models m0_{sb} and m1_{sb} refer to the starburst (+shocks), we adopted the same relative abundances as those adopted in the pl radiation dominated models in order to obtain a rough fit to the observed [OII] and [OIII] line ratios to H β .

We could not find any shock dominated model ($F=0$, $U=0$) which could consistently reproduce the [OII]/H β and [OIII]/H β line ratios as can be noticed from Table A1. These results indicate that in NGC 6240 the shock contribution is always combined with that of radiation.

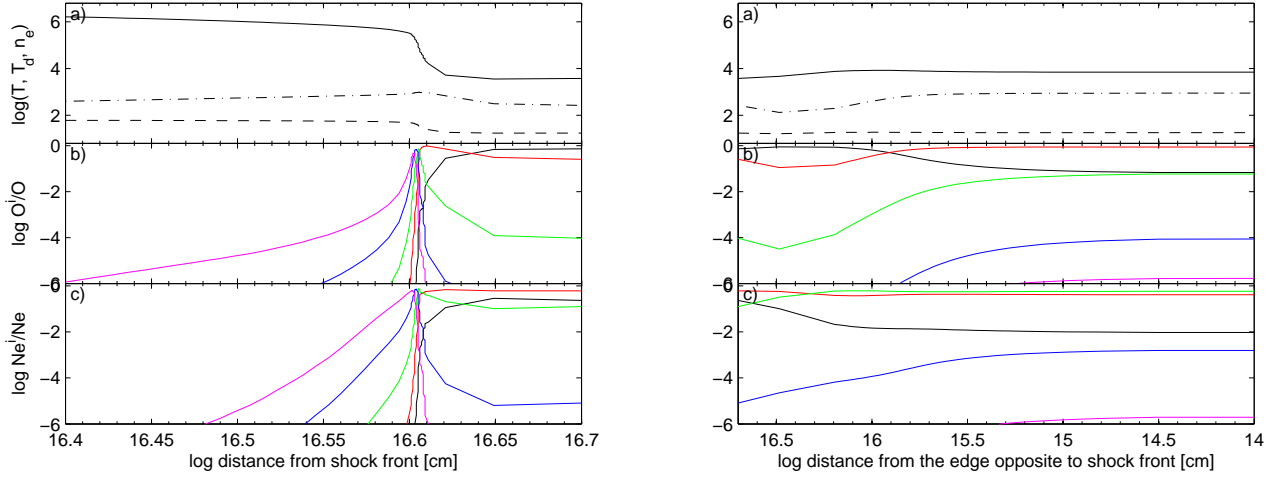


Figure 2. The physical conditions throughout a cloud corresponding to model $m2_{pt}$ (Table 1). The shock front is on the left of the left diagram; the cloud edge reached by the flux from the AGN is on the right of the right diagram (see text). Top panel : T (solid line) , T_d (dashed line), n_e (dot-dashed line) . Middle panel : The fractional abundance of the oxygen ions : black : O^0/O ; red : O^+/O ; green : O^{++}/O ; blue : O^{3+}/O ; magenta : O^{4+}/O . Bottom panel : the same as the middle panel for Ne ions.

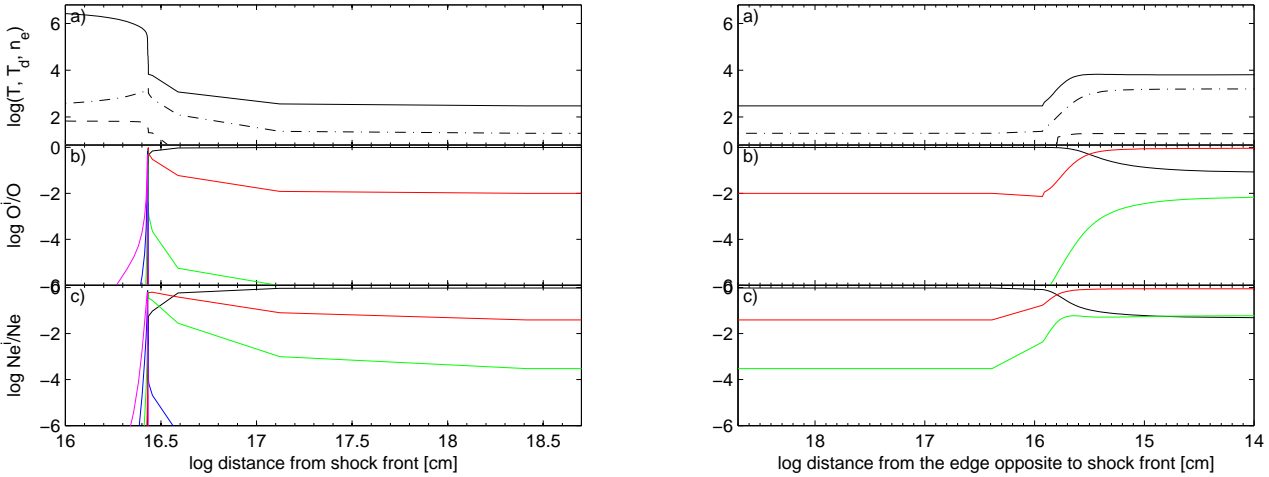


Figure 3. The same as for Fig 2 for a cloud corresponding to model $m1_{sb}$ (Table 1).

To better understand the line ratios calculated by the models, we present in Figs. 2 and 3 the distribution of the temperature T (in K), electron density n_e (in cm^{-3}) and grain temperature T_d (in K) in the top panels. The fractional abundance of oxygen and neon ions throughout a cloud which propagates outward from the AGN are shown in the middle and bottom panels, respectively. In Fig. 2 the radiation flux reaching the cloud is a power-law characteristic of AGNs. In Fig. 3 the cloud is ejected from the starburst. The radiation flux is a black-body. The clouds in both Figs. 2 and 3 are divided into two halves represented by the left and right diagrams. The shock front is on the left of the left diagram, while the radiation flux reaches the opposite edge (right edge of the right diagram). The left diagram represents the region downstream close to the shock front and the X-axis scale representing distance from shock front, is logarithmic. The right diagrams show the conditions downstream far from the shock front, close to the edge illuminated

by the radiation flux. The distance from the illuminated edge is given by a reverse logarithmic X-axis scale. Thus the conditions throughout a cloud are seen with critical resolutions at the two edges.

The calculations show that the maximum temperatures in the immediate post-shock region downstream (Figs. 2 and 3, top panel) result $1.2 \cdot 10^7$ K and $3.75 \cdot 10^6$ K for $V_s = 900$ km s^{-1} and $V_s = 500$ km s^{-1} , respectively, leading to X-ray emission (Fig. 4). The cooling rate downstream determines the distribution of the electron densities and temperatures, and consequently, the intensity of the emission lines and of the continuum.

In composite models for outflowing clouds (Figs 2 and 3, middle panel), $[\text{OIII}]/[\text{OII}]$ line ratios are higher from the photoionised side of the cloud because radiation heats the gas at temperatures of $2\text{--}3 \cdot 10^4$ K which are suitable to the $[\text{OIII}]$ line ionization potential. Nevertheless, for NGC 6240 $[\text{OIII}]/[\text{OII}] < 1$, because F is relatively low. The

[OII]/[OIII] and [OI]/[OIII] ratios are higher from the shock front edge because the temperature drop characteristic of shock dominated models leads to a large region of gas at $T \leq 10^4$ K, adapted to strong [OII] and [OI] lines. The two sides are bridged by secondary radiation which maintains the gas at about 10^4 K. So in NGC 6240 the shock dominates, but photoionization cannot be neglected, in particular because the AGN are observed.

Modelling the line ratios, we had to exclude preshock densities higher than $40\text{--}60\text{ cm}^{-3}$ and d/g ratios higher than $4 \cdot 10^{-3}$ because they did not improve the fitting of the line spectrum and continuum SED (Table A1). The cooling rate by line and continuum emission of the gas is $\propto n^2$ and the cooling rate by collisionally heating of dust grains is $\propto d/g$ (Dwek 1987). Higher densities and higher d/g speeding up the cooling rate downstream by a constant factor will change the distribution of the fractional ions (Contini 2004b). The emitted spectrum will change accordingly.

Moreover, oxygen and carbon are strong coolants (we cannot refer here to He whose lines were not observed), namely, the cooling rate depends also on the O/H and C/H relative abundances. Adopting C/H solar or slightly higher than solar ($3.3\text{--}4.3 \cdot 10^{-4}$) and O/H higher than solar ($8.6 \cdot 10^{-4}\text{--}9.6 \cdot 10^{-4}$) the calculation results were acceptable. In fact higher relative abundances increase the cooling rate only in the zones downstream where the gas reaches the conditions adapted to emit strong lines, i.e. not constantly throughout the whole downstream region.

Notice that O/H values are higher than solar referring to Asplund et al. (2009), Allen (1976), and Anders, Grevesse (1989), who give O/H = 4.9 - 6.6 - $8.5 \cdot 10^{-4}$, respectively. Relatively high [NII] 6548+/H β ratios, fitting the data, were calculated by models adopting N/H = 1.5 solar. The [NeIII]/H β line ratio is overpredicted by the models $m1_{pl}$ and $m2_{pl}$ because the calculations account for both the $\lambda 3869$ and $\lambda 3940$ lines, while the observations refer only to the $\lambda 3869$ line. Finally, relatively high [OI]/H β and [NI]/H β line ratios result generally from pl radiation-bound dominated models (see Contini 2004a).

3.2.2 The infrared lines

In the second panel of Table 1, the infrared line ratios reported by Armus et al (2006) are shown. They presented flux and FWHM of fine-structure narrow lines observed from NGC 6240. The NGC 6240 line fluxes reported by Dasyra et al (2011) who collected mid-IR lines of type 2 Seyfert galaxies for [SIV]10.5, [NeII]12.8, [NeV]14.3, [OIV]25.9, [NeIII]15.5 and [OIV]25.9 from the *Spitzer* catalog correspond to those of Armus et al. The lines are generally the strongest in the IR range (see Figs. 2 and 3). They refer to three ionization levels of Ne, constraining the models.

We show in Table 1 the observed line ratios to [NeII] 12.8, which are independent from the neon relative abundance, at least two of them, and we compare them with the results of models which were selected by the fit of the optical spectrum. The [NeII] absolute fluxes are also shown in the last row of the Table 1 second panel, both observations at Earth (col. 2) and models calculated at the nebula (col. 3-8).

We first refer to the lines reported in the survey

of Dasyra et al. The data are reproduced by 2 - 42 % by the starburst dominated model ($m1_{sb}$) which appears in column 7 of Table 1. The spectra dominated by a power-law radiation flux overpredict by a factor > 6 the [NeIII]15.5/[NeII]12.8 line ratio. Our results show that, on the contrary, the starburst model ($m1_{sb}$) reproduces the infrared line ratios within 43 %. Recall that although the [OIII]5007/H β and [OII]/H β line ratios were reproduced within the observational error by the starburst models, the neutral optical lines were underpredicted by factors of 3 up to >10 , suggesting that even if starbursts are present, the neutral lines emitted by the surrounding clouds are too weak to be observed.

If we refer only to the IR lines, both inflow and outflow models are valid, however, if we consider also their contribution to the optical lines, indeed the inflow model should be dropped because underpredicting the [NeIII] 3869/H β and the [OI]6300/H β line ratios by factors > 50 . A more physical constraint consists in the starburst super-wind indicated by Heckman et al. Moreover, the blue wings of [NeV] and [OIV] seems redshifted relative to [NeII] and [NeIII] profiles (Dasyra et al 2011).

We consider now the S, Si, Ar and Fe lines presented by Armus et al. The [ArII]/H β ratio is reproduced by Ar/H twice solar. Ar is not trapped into dust grains because of its atomic structure, while Si, S and Fe can be included in grains and molecules. We have run model $m2_{sb}$ representing outflow from the starburst and depleted elements. The input parameters were slightly modified in order to save the good fit to the optical line ratios. The results which are given in column 8 of Table 1, show that the IR [SIII] lines are overpredicted by the model by a factor >2 , while the optical [SII] lines are underpredicted by a factor of 4.6 adopting S/H=4. 10^{-6} (0.25 solar). This indicates that the optical and IR sulphur lines come from different regions and that in the IR line emitting region sulphur is trapped deeply into molecular clouds.

In the third panel of Table 1 the [CII] absolute flux presented by Luhman et al (1998) is reported. The absolute fluxes are calculated by the models adopted to calculate the other IR lines. Luhman et al claim that [CII] fluxes are very low for NGC 6240 (and for Arp 220) and that NGC 6240 shows a [CII]/ FIR continuum ratio consistent with starburst nuclei.

In the bottom panel of Table 1 the input parameters are shown. The high V_s adopted by the models to fit the observed FWHM of the line profiles, confirm that shocks have a leading role in NGC 6240. The starburst dominated models indicate that a relatively low ionization parameter U , diluted by distance, is consistent with a large geometrical thickness D of the emitting cloud.

Summarizing, the results of modelling presented in Table 1 show that the AGNs dominate the optical spectrum, while the starbursts better explain the IR lines. The emitting nebulae are most probably located in different regions.

In the last column of Table 1 we show the averaged line ratios obtained by summing up model $m2_{pl}$ and model $m2_{sb}$ with relative weights of 0.3 and 0.7 respectively. The fit of some line ratios to the data improve, but not for all the lines. In fact, different lines are emitted from different regions of the galaxy, so a real picture should account for many different conditions.

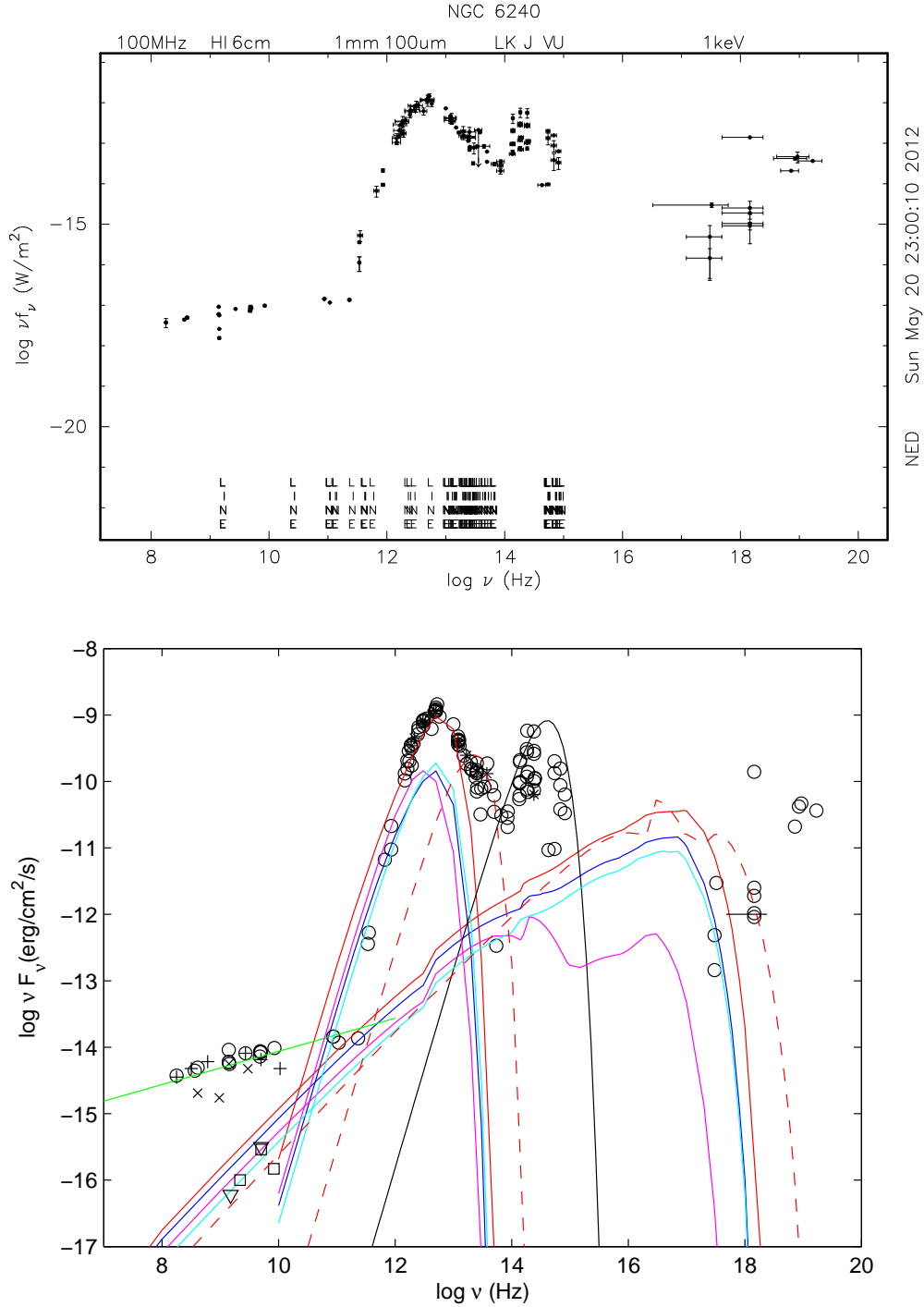


Figure 4. The SED of the continuum. The data are explained in the text. Blue lines : model $m2_{pl}$; red lines : $m1_{pl}$; magenta lines : $m0_{sb}$; cyan lines : $m1_{sb}$; red dashed lines : model calculated by $V_s = 2000 \text{ km s}^{-1}$ and $n_0 = 500 \text{ cm}^{-3}$; green line : synchrotron radiation; black line : black body flux from background stars.

4 THE CONTINUUM SED

NGC 6240 is a luminous infrared galaxy. This can be noticed through the continuum SED which is composed by the very rich set of observations, covering the frequency range from radio to X-rays (Fig. 4, top panel).

The data from the NED (Large et al. 1981, Condon et al. 2002, White, Becker 1992, Condon et al. 1996, Wright,

Otrupcek 1990, Bennett et al. 1986, Griffith et al. 1995, Laine et al. 2006, Nakanishi et al. 2005, Iono et al. 2007, Wilson et al. 2008, Yang, Phillips 2007, Benford 1999, Spinoglio et al. 2002, Negishi et al. 2008 Brauher et al. 2008, Moshir et al. 1990, Lahuis et al. 2007, Armus et al. 2006, Egami et al. 2006, Golombek et al. 1988, Sanders et al. 2003, Siebenmorgen et al. 2004, Klaas et al. 2001, Forster et al. 2004, Veilleux

et al. 2009, Marshall et al. 2007, Allen 1976, 2MASS. 2003, Rudy et al. 1982, Spinoglio et al. 1995, De Vaucouleurs, Longo 1988, De Vaucouleurs et al. 1991, Gonzalez-Martin et al. 2009, Brinkmann et al. 1994, Lutz et al. 2004, Gonzalez-Martin et al. 2006, Beckmann et al. 2009, Sazonov et al. 2007, Gower et al. 1967) are represented in the bottom panel of Fig. 4 by open circles.

Even if the NED data are taken with different apertures and at different times, Fig. 4 shows that they very consistently follow the trend of a power-law flux (synchrotron radiation) in the radio frequency range, a composite black-body infrared emission from dust in the IR, the black body radiation in the optical-near-UV which bounds the fluxes of the old star population. Moreover, they indicate X-ray emission in the soft and hard energy ranges.

We have added the data in the radio observed by Hagiwara et al (2011) from the northern source N2, which shows the strongest fluxes at epochs 2003-October-November (open triangles) and 2009-June (open squares). Hagiwara et al used the European Very Long Baseline Interferometry Network. The + and x refer to the low resolution observations and the flux densities seen in the interferometer observations by the Cambridge One-Mile Telescope (COMT) and the Jodrell Bank Interferometers (JBI) and Cambridge 5-km telescope (FW79 and references therein), respectively. The errorbars of the latter are large, particularly for the datum at 10^4 MHz. We have omitted the errorbars from all the data in all the ranges far sake of clarity in the bottom diagram of Fig. 4 in which we compare the data with model calculations. We have also added the Spitzer IR data presented by Sargsyan et al. (2011) (collected from the *AKARI* catalog, from the *IRAS* Faint Source Catalog and from the 2Mass Catalog) which are indicated by the asterisks. The models which were selected by the fit to the line spectra are used to reproduce the continuum SED.

The data in the radio from the NED agree with COMT observations (FW79). They follow the trend of the calculated synchrotron radiation flux emitted by the Fermi mechanism at the shock front (Bell 1978). However the JBI data (FW79) show a slightly steeper trend and lower fluxes intensities. The trend of the Hagiwara (2011) data is definitively different, following the bremsstrahlung calculated by the models presented in Table 1. Moreover, the Hagiwara data are lower by a factor of > 10 .

The most reasonable explanation is that the data from the NED and from COMT refer to a large area and embrace the clouds shocked by the starburst super-wind (Heckman et al 1990). The data from the NED are broad band observations, mostly integrated from maps. Not only radio - optical- UV radiation will be emitted from the clouds, but being carried by the super-wind, radio synchrotron radiation will be emitted at the shock fronts and X-rays at the shocked edges. As the starburst fills the whole region between the AGNs and beyond, the same is valid for clouds photoionised by the pl radiation. On the other hand, Hagiwara observations are focused towards a well defined region. So most probably, we see only the bremsstrahlung from the photoionised edge of the clouds.

The far IR fluxes come from different regions in different conditions. Notice, for example, that in the millimetric at the same frequency ($\sim 3 \cdot 10^{11}$ Hz) the synchrotron radio tail and the reradiation by dust appear from different obser-

vations. Moreover, the data between $\sim 10^{14}$ and $> 10^{15}$ Hz are nested within the Planck function representing the old star ($T=4000$ K) background.

Tezca et al (2000) wonder about the dust heating cause in the IR, namely, by the AGN or by the starburst. In our models clouds reached by radiation from the AGNs and from the starburst are also heated and ionized by the shocks.

As we have explained in sect. 3, the continuum from the models shows the characteristic bremsstrahlung slope at frequencies lower than 10^{14} Hz common to all the models, because emitted from cool gas ($T < 10^3$ K). The slopes between 10^{14} and 10^{15} Hz depend on the flux from the AGN or from the stars which heat the gas to $\sim 3-4 \cdot 10^4$ K, changing from model to model. At higher frequencies the slope is dictated by the shock which can heat the gas at high temperatures depending on V_s (sect. 2). Therefore we have included in Fig. 4 (bottom panel) model $m0_{sb}$ which is calculated by $V_s = 300 \text{ km s}^{-1}$, for comparison.

A higher n_0 will enhance the bremsstrahlung which is $\propto n^2$. In Fig. 4 we refer in particular to the SED of the continuum. The models, which are calculated from the emitting gas, are shifted on the Y-axis in order to reproduce the observed data at Earth. The shift is proportional to r^2/d^2 , where r is the distance of the gas nebula from the AC and d is the distance of the galaxy from Earth. So we find $r=5$ kpc for the clouds ionized by the AGN radiation downstream of a shock with $V_s = 500 \text{ km s}^{-1}$, $r=5.4$ kpc for the clouds ionized by the AGN and $V_s = 900 \text{ km s}^{-1}$ and $r=3$ kpc for the clouds ionized by the starburst.

We have run a shock dominated ($F=0$) model with $V_s = 2000 \text{ km s}^{-1}$ and $n_0 = 500 \text{ cm}^{-3}$, $a_{gr} = 0.5 \mu\text{m}$, $d/g = 0.002$ by mass. The calculated SED nicely fits the data in the soft-X-ray range and completes the modelling of the IR reprocessed emission. The maximum temperature reached by the grains is $T_{gr} = 288$ K. These high velocity clouds would be located at $r = 97$ pc from the galaxy centre. This model contributes only to high ionization lines ([FeVII], [FeX], etc.). It contributes by less than 10% to the spectra calculated by the starburst model and less than 1% to the pl calculated lines presented in Table 1.

Dust reprocessed radiation in the IR is calculated consistently with gas emission by the mutual heating and cooling of grains and gas atoms. Collisional processes dominate at the high temperatures which refer to the relatively high shock velocities in NGC 6240. Therefore, dust grains would be heated collisionally by the gas to relatively high temperature at the cloud shock front edge, but here the grains are easily sputtered for shock velocities $V_s > 200 \text{ km s}^{-1}$. Adopting $a_{gr} = 1 \mu\text{m}$ in the present models, the grains are reduced by sputtering to $\sim 0.5 \mu\text{m}$. The maximum temperature of dust for model $m1_{pl}$ is $T_d = 81$ K and for model $m1_{sb}$ is $T_d = 68$ K. The models were calculated adopting $d/g = 4 \cdot 10^{-3}$ by mass.

Armus et al in their analysis of the continuum SED, refer to three dust components at 27.1 ± 0.3 K (cold), at 81.4 ± 1.8 K (warm) and at 680 ± 12 K (hot) in order to reproduce the IR dust reprocessed bump. Our results agree with the warm temperature, but the hot temperature is much lower. The cold temperature is included in the calculations reproducing the warm one. Indeed, the model adopted by Armus et al about grain properties and location is different from our which accounts for collisional heating of the grains.

Moreover, dust emission is calculated consistently by models that are constrained by the spectra emitted from the gas.

Komossa et al claim that a large part of the X-ray is extended. Soft X-rays are emitted downstream of shocks with the characteristic velocities ($500\text{--}900\text{ km s}^{-1}$) that were calculated by modelling the line spectra. The shocks accompany the outward motion of the clouds carried by the superwind. The starburst embraces a large region, therefore the soft X-ray emission is spread throughout the galaxy.

CHANDRA data are integrated between 2–10 keV (Fig. 4, top panel). Although soft-X-ray data are explained by bremsstrahlung emitted by the high velocity gas, hard X-rays are hardly reproduced by the bremsstrahlung from gas in the conditions suitable to explain the optical-IR line spectra. In fact X-ray observations at 2–10 keV reveal the presence of iron line emission at 6.4 keV from both nuclei, which is most prominent in the southern nucleus and classifies this galaxy as a binary AGN (Hagiwara et al 2011, Komossa et al 2003). The strong Fe K α line is not produced in a starburst superwind but originates in cold material illuminated by a hard continuum spectrum.

5 DISCUSSION AND CONCLUDING REMARKS

The Seyfert galaxy NGC 6240 is the result of collision and merging. Merging objects generally include 1) a double active nucleus, 2) stars and starbursts in the central region and in the edges, even beyond them, and 3) shocked fragmented clouds. Therefore, the models adopted for the calculation of the spectra account for the power-law radiation flux from the AGNs, black-body radiation flux from the starburst and shock waves.

We have calculated the physical conditions throughout the galaxy by modelling the optical, infrared line ratios and the continuum SED. The best fitting models were selected from a large grid.

5.1 The physical picture

Modelling suggests that the clouds photoionised by both the AGN flux and by the starburst move outwards, i.e. they are not gravitationally falling towards the black holes. The starburst region embraces the zone between the AGNs and beyond it and a starburst super-wind carries the clouds outwards (Heckman 1990).

We have found that the flux from the AGN (or AGNs) F is similar to the lowest ones found in LINERs (e.g. Contini 1997) and LLAGNs (e.g. Contini 2004a). It leads to optical line ratios best fitting the data. The pl radiation flux photoionises the clouds and heats the gas at maximum temperatures of $3\text{--}4\text{ }10^4\text{ K}$. The gas is mainly heated by the shock to maximum temperatures of $3.75\text{ }10^6\text{ K}$ and $1.2\text{ }10^7\text{ K}$ accompanying the clouds outwards with shock velocities $V_s \sim 500\text{--}900\text{ km s}^{-1}$, respectively. A high V_s combined with a low n_0 ($\sim 40\text{ km s}^{-1}$) leads to the high [OII]/[OIII] observed in NGC 6240.

A distance $r \sim 370\text{ pc}$ from the AC is calculated for the gas reached by the AGN radiation and emitting the observed optical line ratios, combining the $H\beta$ absolute flux calculated at the nebula by model $m2_{pl}$ (Table 1) with $H\beta$ observed at

Earth : $H\beta_{abs} r^2 = H\beta_{obs} d^2$, where d is the distance from Earth and $H\beta_{obs} = 1.7\text{ }10^{-14}\text{ erg cm}^{-2}\text{ s}^{-1}$ (FW97). The distance r is a lower limit. A higher distance should result accounting for the filling factor, $f = 10^{-3} - 10^{-4}$ (Heckman et al 1990). The results obtained for r by modelling the continuum in Sect. 4 lead to $f = 0.074$.

The infrared spectrum reveals the starburst. We have found that the IR line ratios are emitted from gas photoionised by a starburst corresponding to a stellar colour temperature $T_* \sim 5\text{ }10^4\text{ K}$. The gas is included in geometrically thick clouds ($D = 3\text{ pc}$). The ionization parameter is low ($U = 0.002$), indicating that the starburst region is extended and the photon flux is diluted on its way to the emitting gas.

In Fig. 5 we plot [NeV]/[NeII] versus [NeIII]/[NeII] for both the Type I and Type II AGN samples of Dasyra et al (2011). We chose only Ne lines in order to avoid the relative abundance problem. Fig. 5 shows that the two samples almost coincide, suggesting that the AGN is not the main source of ionization. Indeed the starbursts and the shocked gas throughout the NLR dominate, as also appears by comparing NGC 6240 with the AGN samples in Fig. 5.

The clouds emitting the [NeII] 12.8 lines are at a distance $r \geq 4.3\text{ kpc}$ from the starburst, which is calculated by combining the [NeII] absolute flux calculated by model $m1_{sb}$ (Table 1) with [NeII] observed at Earth (Dasyra et al 2011) : $[NeII]_{abs} r^2 = [NeII]_{obs} d^2$, where d is the distance of NGC 6240 to Earth. A distance of 4.3 kpc was found comparing the calculated to the observed continua, leading to $f \leq 1$.

The models presented in Table 1 are constrained enough to allow to calculate the location of the [CII] emitting region. Combining the flux observed at Earth with that calculated at the nebula, we obtain $r = 9\text{ kpc}$ for the AGN (by model $m2_{pl}$) and 11 kpc for the starburst (by model $m2_{sb}$), adopting a filling factor of 1.

We found in agreement with FW97 that the preshock densities are relatively low ($< 100\text{ cm}^{-3}$) compared to those calculated in the NLR of Seyfert galaxies ($> 100\text{ cm}^{-3}$), but higher than those of the ISM ($> 1\text{ cm}^{-3}$). The preshock densities are relatively low in both the clouds ionised by the starburst and by the AGN. The characteristic low density in the NLR of NGC 6240 suggests that the gas from the ISM was inflated inside the colliding galaxies and mixed up, diluting their former densities. Alternatively, both the colliding galaxies were characterised by low density gas similar to that found near the centre of the Milky Way.

The shock velocities are relatively high ($V_s = 500\text{--}900\text{ km s}^{-1}$) and similar for most of the clouds which are carried by the wind, confirming that the high shock velocities arise from an extended collision event. They are slightly higher than the observed FWHM of the lines ($\sim 400\text{ km s}^{-1}$), indicating that shocks are stronger than the bulk velocity of the clouds in some positions.

The similarity of some of the physical conditions predicted by the AGN and starburst models (e.g. low densities, high velocities and relative abundances slightly higher than solar) is peculiar, indicating that the clouds are most probably remnants of shells ejected from the starburst. The matter swept up by the blast wave accelerates outward and fragments via Rayleigh-Taylor instabilities. Relatively small geometrical thickness of the clouds ($D = 0.03 - 0.2\text{ pc}$) are calculated in the neighbourhood of the AGNs. However, they

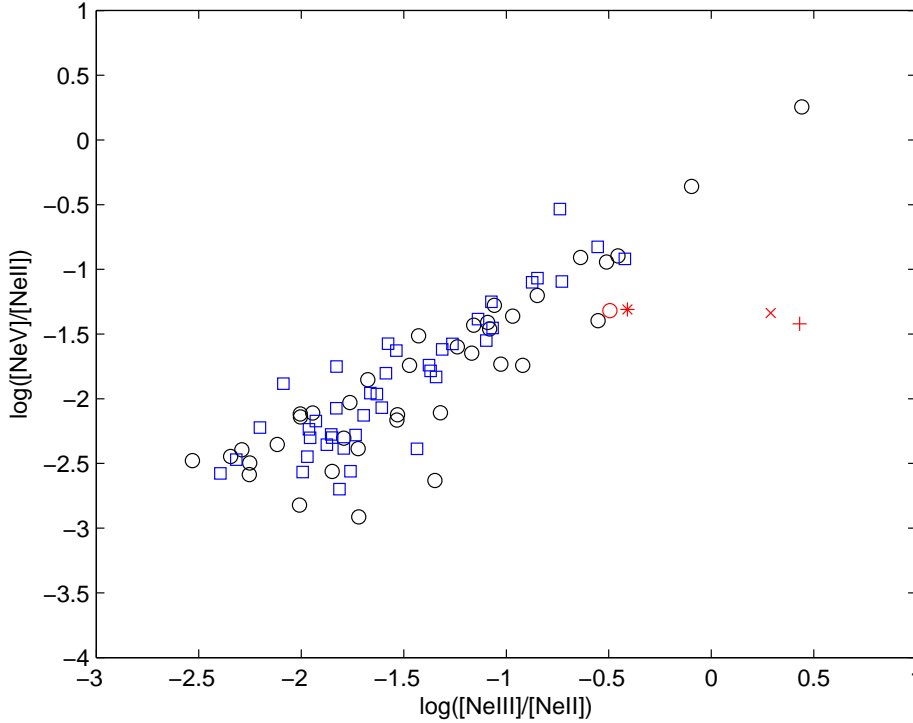


Figure 5. $[\text{NeV}]/[\text{NeII}]$ versus $[\text{NeIII}]/[\text{NeII}]$ for the sample of Type 1 and Type 2 AGN presented by Dasyra et al. (2011) : blue squares and black circles, respectively. The red circle represents NGC 6240; the red asterisk indicates the starburst model result. Red + and red X represent the AGN models calculated by $V_s = 500 \text{ km s}^{-1}$ and 900 km s^{-1} , respectively.

are large enough to include a large zone of neutral gas (Fig. 3). Here, the electron temperature and densities are kept relatively high by the secondary radiation, so the neutral emission lines ($[\text{NI}]$ and $[\text{OI}]$) are high enough to fit the observed $[\text{NI}]/\text{H}\beta$ and $[\text{OI}]/\text{H}\beta$ line ratios. The clouds which better reproduce the infrared line spectrum are ionised by the starburst and have geometrical thickness ($D = 3 \text{ pc}$) higher by a factor ≥ 10 . Neutral line ratios are lower than in the clouds close to the AGNs, due to a large region of cold gas inside the cloud. Different geometrical thickness are in agreement with an underlying turbulence (Contini & Goldman 2011)

5.2 Relative abundances of the heavy elements in the gaseous phase

The influence of merger-induced inflows, enrichment and gas consumption, galactic winds, etc. is important in determining the nuclear metallicity. The central metallicity is primarily a competition between the inflow of low-metallicity gas and enrichment from star formation (Torrey et al 2012).

We have obtained the best fit to the spectra by $\text{C}/\text{H} = 1. - 1.3$ solar, $\text{N}/\text{H} = 1.5$ solar, $\text{O}/\text{H} = 1.45$ solar and Ar is twice solar. The relative abundances derived from our modelling of the NGC 6240 emission spectra are not common in mergers at low z . Before considering enrichment for instance from star formation, let us consider some evidences about grains and molecules in a collision dominated regime such as that in NGC 6240.

Tacconi et al (1999) report the result of the CO $J=2 \rightarrow 1$

line observations. Half of the CO flux is concentrated in a thick disc structure situated between the two radio/infrared nuclei, with a diameter $\leq 500 \text{ pc}$. Strong CO bands were already found in NGC 6240 by Rieke et al (1985) indicating giant and supergiants, where dust is formed. Also H_2 $v=1 \rightarrow 0$ emission is centered between the radio/infrared nuclei (Joseph et al 1984).

Mac Law & Glover (2011) and Glover & Mac Law, (2012) calculations on the formation of H_2 and CO in clouds, show that the CO molecules are easily dissociated for low densities ($\sim 30 \text{ cm}^{-3}$) while H_2 molecules are still present, partially removing H from the gaseous phase. Strong molecular hydrogen emission has been detected by Rieke et al (1985) and by Becklin et al (1984) in NGC 6240.

The $1-0\text{S}(1)\text{H}_2$ emission line is one of the most powerful found in any galaxy to date (Joseph et al 1984), probably excited by shocks (Tecza et al 2000, etc.), while CO abundance around the nuclei is very likely to have been significantly reduced by X-ray irradiation from the AGN. It seems that the H_2 emission is excited purely by thermal mechanisms (Sugai et al 1997) and H_2 lines are emitted between the double nuclei. From its excitation mechanism and its peak position, the emission is from a global shock caused by a galaxy-galaxy collision.

We suggest that abundances of heavy elements relative to H are high in NGC 6240 due to trapping of hydrogen into H_2 molecules, removing it from the gaseous phase. High C/H , N/H , O/H and Ar/H are therefore an indirect record of collision. They do not indicate high metallicities,

but they reveal the formation of H_2 molecules in a large collision event. We cannot predict the true C/H, N/H and O/H relative abundances, perhaps lower than solar. Yet, the remnants of the inflated gas can explain Heckman et al discovery of two very bright knots located about 8.5 kpc west and 2.5 kpc WSW of the nucleus. They have line widths less than 100 km s^{-1} FWHM and $\text{H}\alpha$ is about 15 times brighter than [SII] 6717+ and at least 25 times brighter than [NII] 6584. Heckman et al. claim that these knots are probably giant HII regions with $\text{H}\alpha$ uncorrected luminosities of about 4×10^{39} and $9 \times 10^{39} \text{ erg s}^{-1}$, respectively and that [NII] and [SII] lines suggest very low metal abundances, less than 20% solar. We suggest that they represent the original inflowed matter, not processed by the super-wind.

On the other hand, elements which are easily trapped into grains and molecules are strongly depleted from the gaseous phase. Fe is generally included into small grains and therefore easily sputtered. The depletion of Fe indicates that depleted matter was included at collision of the galaxies. S and Si can be included into molecules, but downstream of shocks at $V_s = 500\text{--}900 \text{ km s}^{-1}$ everything is evaporated. So they were also originally depleted in the included matter, in agreement with Heckman et al.

ACKNOWLEDGEMENTS

I am grateful to the referee for many interesting comments which improved the presentation of the paper. This research has made use of the NASA Astrophysics Data System (ADS) and the NED, which is operated by the Jet Propulsion Laboratory, California Institute of Technology, under contract with NASA.

REFERENCES

- Allen, D.A. 1976, *ApJ*, 207, 367
 Anders E., Grevesse N. 1989, *Geochimica et Cosmochimica Acta* 53, 197
 Armus, L. et al. 2006, *ApJ*, 640, 204
 Asplund M., Grevesse N., Sauval A.J., Scott P. 2009, *ARAA*, 47, 481
 Beck, R. 2011, arXiv:1112.1823
 Becklin, E.E., DePoy, D., Wynn-Williams, C.G. 1984, Paper presented at the Infrared Detector Workshop, Laramie, Wyoming, May 15-16, 1984.
 Beckmann, V. et al. 2009, *A&A*, 505, 417
 Bell, A.R. 1978, *MNRAS*, 182, 147
 Benford, D.J. 1999 vol. Thesis p. 1
 Bennett, C.L., Lawrence, C.R., Burke, B.F., Hewitt, J.N., Mahoney, J. 1986, *ApJS*, 61, 1
 Brauher, J. R.; Dale, D. A.; Helou, G. 2008, *ApJS*, 178, 280
 Brinkmann, W., Siebert, J., Boller, Th. 1994, *A&A*, 281, 355
 Condon, J.J., Helou, G., Sanders, D.B., Soifer, B.T. 1996, *ApJS*, 103, 81
 Condon, J.J., Cotton, W.D., Broderick, J.J. 2002, *AJ*, 124, 675
 Contini, M. 2012, arXiv:1206.3060
 Contini, M., Cracco, V., Ciroi, S. 2012, *A&A*, submitted
 Contini, M., Goldman, I. 2011, *MNRAS*, 411, 792
 Contini, M. 2009, *MNRAS*, 399, 1175
 Contini, M. 2004a, *MNRAS*, 354, 675
 Contini, M. 2004b, *A&A*, 422, 591
 Contini, M., Viegas, S.M. 2001 *ApJS*, 132, 211
 Contini, M.; Viegas, S. M.; Prieto, M. A. 2004, *MNRAS*, 348, 1065
 Contini, M. 1997, *A&A*, 323, 71
 Contini, M., Aldrovandi, S.M. 1983, *A&A*, 127, 15
 Cox, D.P. 1972, *ApJ*, 178, 169
 Dasyra, K.M. et al. 2011, *ApJ*, 740, 94
 De Vaucouleurs, A., Longo, G. 1988, Catalogue of visual and infrared photometry of galaxies from 0.5 micron to 10 micron (1961-1985)
 De Vaucouleurs, G., De Vaucouleurs, A., Corwin JR., H.G., Buta, R. J. Paturel, G., Fouque, P., 1991, Third reference catalogue of bright galaxies, version 3.9
 Diaz, A.I., Prieto, M.A., Wamsteker, W. 1988, *A&A*, 195, 53
 Dwek, E. 1987, *ApJ*, 322, 812
 Egami, E., Neugebauer, B., Soifer, B.T., Matthews, K., Becklin, E.E., Ressler, M.E. 2006, *AJ*, 131, 125
 Engel, H. et al. 2010, *A&A*, 524, 56.
 Feldman U. 1992, *Physica Scripta* 46, 202
 Forster, N.M., Schreiber, Roussel, H. Sauvage, M., Charmandaris, V. 2004, *A&A*, 419, 501
 Fosbury, R.A.E., Wall, J.V. 1979, *MNRAS*, 189, 79
 Fried, J.W., Schulz, H. 1983, *A&A*, 118, 166
 Glover, S.C.O., Mac Low, M.-M 2011, *MNRAS*, 412, 337
 Gallimore, J.F., Beswick, R. 2004, *AJ*, 127, 239
 Genzel, R. et al 1998, *ApJ*, 498, 579
 Golombek, D., Miley, G.K., Neugebauer, G. 1988, *AJ*, 95, 26
 Gonzalez-Martin, O.; Masegosa, J.; Marquez, I.; Guainazzi, M.; Jimenez-Bailon, E., 2009, *A&A*, 506, 1107
 Gonzalez-Martin, O.; Masegosa, J.; Marquez, I.; Guerrero, M. A.; Dultzin-Hacyan, D. 2006, *A&A*, 460, 45
 Gower, J.F.R., Scott, P.F., Wills, D. 1967, *Mem. R. A. S.*, 71, 49
 Griffith, M.R., Wright, A.E., Burke, B.F., Ekers, R.D. 1995, *ApJS*, 97, 347
 Hagiwara, Y., Baan, W.A., Klöckner, H.-R. 2011, *AJ*, 142, 17
 Heckman, T.M., Armus, L., Miley, G.K. 1990, *ApJS*, 74, 833
 Joseph, R.D., Wright, G.S., Wade, R. 1984, *Nature*, 311, 132
 Klaas, U. et al. 2001, *A&A*, 379, 823
 Komossa, S., Burwitz, V., Hasinger, G., Predehl, P., Kaasstra, J.S., Ikebe, Y. 2003, *ApJ*, 582, L15
 Iono, D. et al. 2007, *ApJ*, 659, 283
 Laine S., Kotilainen, J.K., Reunanen, J., Ryder, S.D., Beck, R. 2006, *AJ*, 131, 701
 Lahuis, F. et al. 2007, *ApJ*, 659, 296
 Large, M.I., Mills, B.Y., Little, A.G., Crawford, D.F., Sutton, J.M. 1981, *MNRAS*, 194, 693
 Luhman, M.L. et al. 1998, *ApJ*, 504, L11
 Lutz, D.; Maiolino R.; Spoon, H.; Moorwood, F. 2004, *A&A*, 418, 465
 Mac Low, M.-M., Glover, S. C.O. 2012, *MNRAS*.tmp.2154
 Marshall, J. A.; Herter, T. L.; Armus, L.; Charmandaris, V.; Spoon, H. W. W.; Bernard-Salas, J.; Houck, J. R. 2007, *ApJ*, 670, 129
 Moshir, M. et al 1990 vol. p.
 Nakanishi, K., Okumura, S. K., Kohno, K., Kawabe, R., Nakagawa, T. 2005, *PASJ*, 57, 575

Negishi, T., Onaka, T., Chan, K.-W., Roellig, T.L. 2008, ApJS, 178, 280

Osterbrock, D.E. 1989 in Astrophysics of gaseous nebulae and active galactic nuclei. / University Science Books, 1989

Radovich, M., Ciroi, S., Contini, M., Rafanelli, P., Afanasiev, V. L., Dodonov, S. N. 2005, A&A, 431, 813

Rieke, G.H., Cutri, Roc M., Black, J.H., Kailey, W.F., McAlary, C.W. Lebofsky, M.J., Elston, R. 1985, 290, 116

Rigopoulou, D., Spoon, H. W. W., Genzel, R., Lutz, D., Moorwood, A. F. M., Tran, Q. D. 1999, AJ, 118, 2625

Rodríguez-Ardila, A.; Contini, M.; Viegas, S. M. 2005, MN-RAS, 357, 220

Rudy, R. J., Levan, P. D., Rodriguez-Espinosa, J. M. 1982, AJ, 87, 598

Sanders, D.B., Mazzarella, J.M., Kim, D. -C., Surace, J.A., Soifer, B.T. 2003, AJ, 126, 1607

Sargsyan, L., Weedman, D., Lebouteiller, V., Houck, J., Barry, D., Hovhannisyan, A., Mickaelian, A. 2011, ApJ, 730, 19

Sazonov, S.; Revnivtsev, M.; Krivonos, R.; Churazov, E.; Sunyaev, R. 2007, A&A, 462, 57

Siebenmorgen, R., Krugel, E., Spoon, H.W.W. 2004, A&A, 414, 123

Spinoglio, L., Andreani, P., Malkan, M.A. 2002, ApJ, 572, 105S

Spinoglio, L., Malkan, M.A., Rush, B., Carrasco, L., Recillas-Cruz, E. 1995, ApJ, 453, 616

Sugai, H., Malkan, M.A., Ward, M.J., Davies, R.I. and McLean, I.S. 1997, ApJ, 481, 186

Tacconi, L.J., Genzel, R., Tecza, M., Gallimore, J.F., Downes, D., Scoville, N.Z. 1999, ApJ, 524, 732

Tecza, M., Genzel, R., Tacconi, L.J. et al. 2000, ApJ, 537, 178

Torrey, P., Cox, T.J., Kewley, L., Hernquist, L. 2012, ApJ, 746, 108

Veilleux, S. et al. 2009, ApJS, 182, 628

Viegas, S. M., Contini, M., Contini, T. 1999, A&A, 347, 112

Weaver, K. A. et al. 2010, ApJ, 716, 1151

White, R.L., Becker, R.H. 1992, ApJS, 79, 331

Wilson, C. D. et al. 2008, ApJS, 178, 189

Wright, A., Otrupcek, R. 1990 Parkes catalogue, 1990, Australia telescope national facility, PKSCAT90, 1990

Yang, M., Phillips, T. 2007, ApJ, 662, 284

Table A1. The grid of selected models

[OII]/H β 12.3 ¹	[OIII]/H β 1.8 ¹	[OI]/H β 1.41 ¹	V _s ² -	n ₀ ³ -	F ⁴ -	str -	D ⁵ -
11.	5.5	1.47	900	40	3.e8	0	1.3
4.6	2.56	0.27	700	40	3.e8	0	1.
7.5	4.6	0.22	500	30	3.e8	0	1.
3.76	2.11	0.2	500	40	3.e8	0	1.
8.3	4.29	0.24	500	40	1.e8	0	1.
19.3	9.48	0.4	500	40	5.e7	0	1.
5.0	2.78	0.3	500	60	3.e8	0	1.
7.	4.25	0.48	500	100	3.e8	0	0.5
19.	11.	0.68	500	100	1.e8	0	0.3
2.9	1.7	0.22	200	150	6.e8	0	0.5
6.7	4.	0.38	200	150	4.e8	0	0.33
8.	4.8	0.4	200	150	3.e8	0	0.5
4.	2.55	0.25	150	200	6.e8	0	0.4
17.	8.2	0.27	150	200	1.e8	0	0.5
12.	4.3	1.2	900	40	3.e8	1	0.6
10.6	4.7	1.34	900	60	3.e8	1	0.6
4.6	1.3	0.7	700	40	1.e9	1	1.
4.7	2.23	0.4	600	40	1.e8	1	1.
5.3	1.8	0.65	600	40	3.e8	1	1.
7.2	1.9	1.17	600	40	1.e9	1	1.
7.	2.15	0.3	500	30	3.e8	1	1.
9.7	4.26	0.46	500	40	3.e7	1	1.
8.6	2.87	1.	500	40	2.e8	1	1.
11.	2.5	3.	500	40	3.e8	1	1.
9.4	2.5	1.3	450	40	3.e8	1	1.
8.6	2.1	1.33	500	40	4.e8	1	1.
0.3	0.25	0.005	500	100	3.e7	1	1.
0.3	0.25	0.034	500	100	1.e8	1	1.
0.38	0.25	0.064	500	100	3.e8	1	1.
7.4	2.3	0.45	200	40	3.e8	1	1.
4.2	1.3	0.95	200	150	1.e8	1	1.
8.	1.2	2.6	200	150	6.e8	1	1.
4.6	1.26	0.48	150	200	1.e8	1	1.
35.	15.7	0.48	600	40	0.0	SD	1.
29.	16.	0.67	500	100	0.0	SD	1.
82.	27.9	0.52	200	40	0.0	SD	1.
90.	35.7	0.66	150	200	0.0	SD	1.

¹ observation data by FW79; ² in km s⁻¹; ³ in cm⁻³; ⁴ in photons cm⁻² s⁻¹ eV⁻¹ at the Lyman limit; ⁵ in 10¹⁷ cm

APPENDIX A: THE MODELS